Lawrence Berkeley National Laboratory

LBL Publications

Title

Mapping Catalytically Relevant Edge Electronic States of MoS2

Permalink

https://escholarship.org/uc/item/9rd0c0vg

Journal

ACS Central Science, 4(4)

ISSN

2374-7943

Authors

Parija, Abhishek

Choi, Yun-Hyuk

Liu, Zhuotong

et al.

Publication Date

2018-04-25

DOI

10.1021/acscentsci.8b00042

Peer reviewed

eScholarship.org Powered by the California Digital Library
University of California

This is an open access article published under an ACS AuthorChoice License, which permits copying and redistribution of the article or any adaptations for non-commercial purposes.

ACS central science

Research Article

Cite This: ACS Cent. Sci. 2018, 4, 493−503

Mapping Catalytically Relevant Edge Electronic States of MoS_2

Abhishek Parija,[†,‡,§] Yun-Hyuk Choi,[†] Zhuotong Liu,[†] Justin L. Andrews,[†] Luis R. De Jesus,[†] Sirine C. Fakra,[§] Mohammed Al-Hashimi,[#] James D. Batteas,[†] David Prendergast,[*,‡] and Sarbajit Banerjee[*,†]

[†]Department of Chemistry and Department of Materials Science and Engineering, Texas A&M University, College Station, Texas 77845-3012, United States

[‡]Molecular Foundry and [§]Advanced Light Source, Lawrence Berkeley National Laboratory, Berkeley, California 94720, United States

[#]Department of Chemistry, Texas A&M University at Qatar, P.O. Box 23874, Doha, Qatar

Supporting Information

ABSTRACT: Molybdenum disulfide (MoS_2) is a semiconducting transition metal dichalcogenide that is known to be a catalyst for both the hydrogen evolution reaction (HER) as well as for hydro-desulfurization (HDS) of sulfur-rich hydrocarbon fuels. Specifically, the edges of MoS_2 nanostructures are known to be far more catalytically active as compared to unmodified basal planes. However, in the absence of the precise details of the geometric and electronic structure of the active catalytic sites, a rational means of modulating edge reactivity remain to be developed. Here we demonstrate using first-principles calculations, X-ray absorption spectroscopy, as well as scanning transmission X-ray microscopy (STXM) imaging that edge corrugations yield distinctive spectroscopic signatures corresponding to increased localization of hybrid Mo 4d states. Independent spectroscopic signatures of such edge states are identified at both the S $L_{2,3}$ and S K-edges with distinctive spatial localization of such states observed in S $L_{2,3}$-edge STXM imaging. The presence of such low-energy hybrid states at the edge of the conduction band is seen to correlate with substantially enhanced electrocatalytic activity in terms of a lower Tafel slope and higher exchange current density. These results elucidate the nature of the edge electronic structure and provide a clear framework for its rational manipulation to enhance catalytic activity.

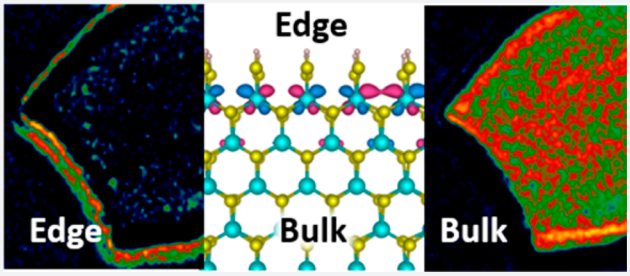

1. INTRODUCTION

The combination of solar energy and water represents the most attractive and fundamentally viable solution to our energy needs if methods can be developed to effectively split water into hydrogen and oxygen.[1−3] Water splitting, the sum of water oxidation and hydrogen evolution half-reactions, remains a formidable challenge since it requires the concerted transfer of four electrons and four protons.[4] Catalysts that can mediate both of the half-reactions at low overpotentials are imperative to avoid squandering valuable free energy harvested using a semiconductor in a photoelectrochemical cell, or provided directly in the form of current in a water electrolyzer. Platinum-group metals are known to effectively catalyze the production of H_2 at low overpotentials; however, their high cost and low crustal abundance has focused attention on the design of more earth-abundant alternatives.[5,6] The 2H polymorph of MoS_2, a semiconducting hexagonally close packed transition metal dichalcogenide, has gained prominence as a catalyst for both the hydrogen evolution reaction (HER)[7−12] as well as for hydro-desulfurization (HDS)[13−16] of sulfur-rich hydrocarbon fuels. Recent reports suggest that it can also electrocatalytically mediate the conversion of higher order lithium polysulfides to solid lower polysulfides.[17] The current understanding from both theoretical[7,18,19] and experimental[8,20−22] approaches is that the catalytic activity of MoS_2 is derived primarily from specific edge sites that are metallic, whereas, in contrast, the basal planes exhibit substantially lower catalytic activity.[23] On the basis of calculations by Tsai and co-workers, the free energy of hydrogen adsorption on the basal plane of MoS_2 is 1.92 eV, which is substantially greater than the 0.06 eV value for the Mo-edges of MoS_2.[24] Furthermore, Voiry and co-workers have demonstrated that the catalytic activity of 2H-MoS_2 is greatly reduced by partially oxidizing the MoS_2 edges, whereas the electrocatalytic performance of the basal plane of 2H-MoS_2 can be somewhat improved by interfacing with carbon nanotubes.[25] Consequently, considerable effort has been invested in increasing the edge density of MoS_2 through precise control of mesoscale structures.[26,27] Despite these advances, the enthalpy of hydrogen adsorption, which is correlated with the overpotential, remains considerably higher for MoS_2 edge sites as compared to Pt.[8,26] As such, a more detailed understanding of the geometric and electronic structure of these sites is required to afford the requisite control to precisely design MoS_2 materials that can function as effective catalysts for water splitting.

Received: January 16, 2018
Published: April 3, 2018

© 2018 American Chemical Society

DOI: 10.1021/acscentsci.8b00042
ACS Cent. Sci. 2018, 4, 493−503

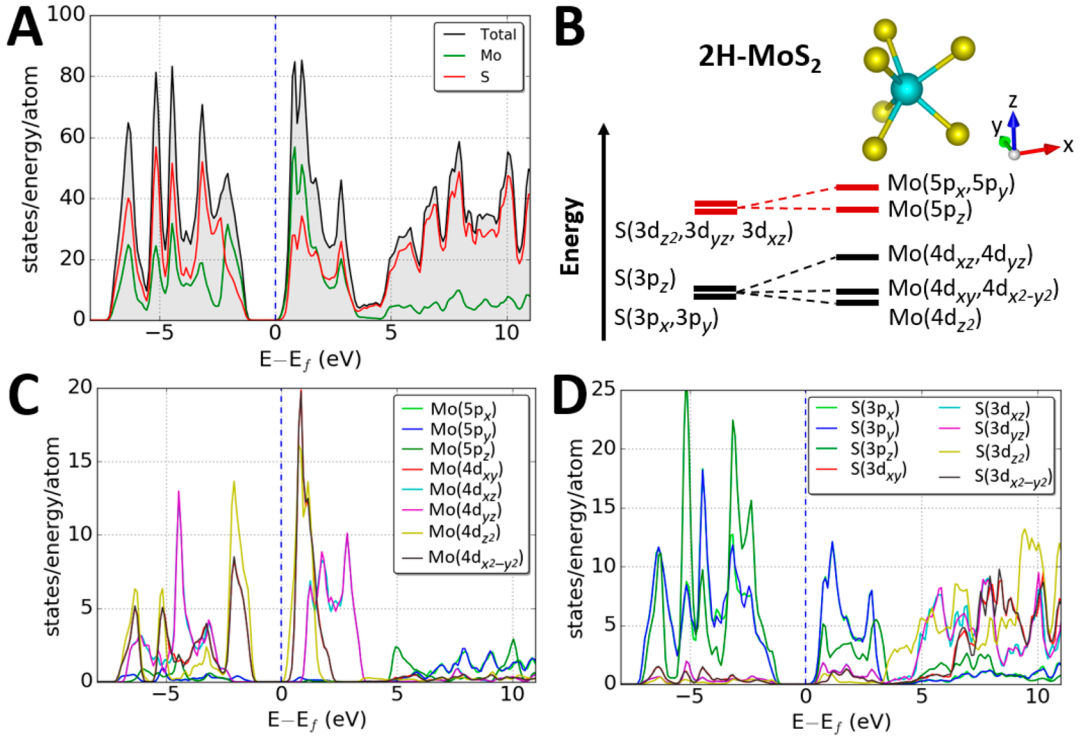

Figure 1. Calculated density of states for a monolayer of 2H-MoS_2. (A) Total density of states and atom-projected density of states plots delineating Mo and S contributions; (B) orbital approximation of the energy levels of the molybdenum and sulfur states and their primary hybridization interactions; the inset depicts the trigonal prismatic local coordination environment of Mo; Mo atoms are depicted as blue spheres, whereas S atoms are depicted as yellow spheres. Orbital-projected density of states for (C) Mo and (D) S atoms in 2H-MoS_2.

Despite considerable research, the precise atomistic structure of the active sites and structure−function correlations of catalytic activity remain unclear in this system,[28] hindering the development of a rational means of modulating the edge reactivity of MoS_2. While scanning tunneling spectroscopy and hyperspectral nano-photoluminescence imaging allow for localized measurements of electronic structure,[29,30] they do not provide an element-specific understanding of specific states mediating catalytic activity. Moreover, these methods have specific length-scale resolution, and probe states without distinct localization or chemical specificity near the band edges that can be rather challenging to interpret theoretically. In this article, we demonstrate that sulfur K- and L-edge X-ray absorption near edge structure (XANES) spectroscopy and imaging serve as sensitive element-specific probes of edge electronic structure. Scanning transmission X-ray microscopy (STXM) measurements at the sulfur $L_{2,3}$-edge of exfoliated MoS_2 samples, an ultrasoft-X-ray elemental edge that has rarely been explored, provide detailed insight into the spatial localization of electronic states based on their distinctive spectroscopic signatures. First-principles density functional theory (DFT) calculations, using the excited electron and core-hole X-ray absorption spectroscopy (XCH-XAS) approach,[31] allow for an orbital-specific description of the origin of the edge electronic states. Remarkably, distinctive spectroscopic signatures are seen as pre-edge absorption features in both S $L_{2,3}$- and K-edge spectra, for specific edge corrugation motifs, and a direct correlation is observed between the density of such sites and the measured electrocatalytic activity. This study thus reveals a direct correspondence between a measured spectroscopic signature (corresponding to a specific symmetry and electronic structure) and macroscopic function, specifically, the electrocatalytic activity of MoS_2, thereby providing a rational means of catalyst design. In other words, a direct correlation between localized chemical bonding motifs and ultimate macroscopic functionality is revealed. Drawing such a correlation is enabling for rational design in terms of parameters such as composition, nano/atomic scale morphology, defect structure, and defect composition/concentration.

2. RESULTS AND DISCUSSION

There is increasing realization of the paramount importance of electronic structure in mediating the electrocatalytic activity of MoS_2 given the need for interfacial charge transfer as well as both electron and proton diffusion.[11,32] A monolayer of 2H-MoS_2 is a semiconductor with a band gap of ca. 1.74 eV with the Fermi level situated just below the conduction band edge.[33] Figure 1 plots the combined density of states (DOS) as well as atom- and orbital-projected densities of states (PDOS) calculated for a 2H-MoS_2 monolayer. The valence and conduction band edges are dominated by hybrid Mo−S states with the orbital-specific interactions schematically illustrated in Figure 1B. Above ca. 4.2 eV, the extent of hybridization is diminished, and the states are predominantly of S character. However, in proximity to the Fermi level, the conduction band edge has hybrid Mo−S character and is split by crystal field splitting effects characteristic of the trigonal prismatic local coordination environment (D_{3h}) of Mo atoms into three distinct envelopes; the lower energy A_1' state has contributions from Mo $4d_{z^2}$ states hybridized with S 3p states, the intermediate energy E′ states comprise $4d_{xy}$ and $4d_{x^2-y^2}$ Mo states hybridized with S 3p states, and the high energy E″ states comprise contributions of Mo $4d_{xz}$ and $4d_{yz}$ origin hybridized with S 3p states (Figure 1C,D). The unoccupied density of

DOI: 10.1021/acscentsci.8b00042
ACS Cent. Sci. 2018, 4, 493−503

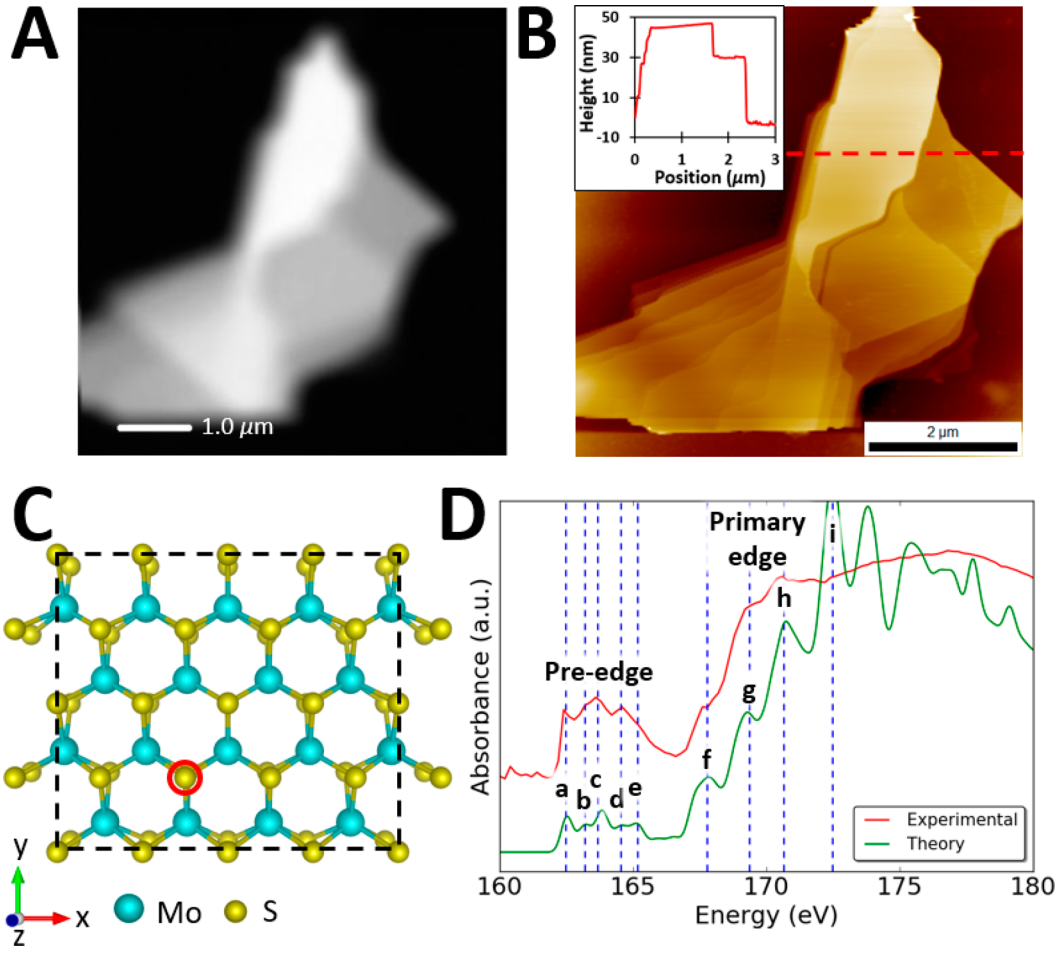

Figure 2. STXM mapping of few-layered 2H-MoS_2. (A) Integrated STXM image (brighter regions correspond to higher absorption) and (B) AFM image for a ca. 45 nm thick 2H-MoS_2 sheet; the inset depicts the cross-sectional topographical profile; (C) supercell of 2H-MoS_2 used to model S $L_{2,3}$-edge X-ray absorption near-edge spectra; the excited sulfur atom is delineated by a red circle. (D) Comparison of experimental and calculated sulfur L-edge XANES spectra of 2H-MoS_2. Final state assignments of the spectral features a—i are detailed in Figure S5 and Table S1 (Supporting Information).

states above ca. 4.2 eV comprises S 3d states split as per the following energy progression owing to hybridization with Mo 5p orbitals $3d_{z^2} < 3d_{xz} = 3d_{yz} < 3d_{xy} = 3d_{x^2-y^2}$ (Figure 1B). Figure S1 (Supporting Information) plots the calculated excited-state density of states for all the S and Mo atoms (including the excited S atom) in 2H-MoS_2. The projected density of states for the specific excited sulfur atom is provided in Figure S2 (Supporting Information). In this calculation, a core−hole is created in the MoS_2 supercell by removing an electron from the 2p orbital of a S atom, and the extra electron is then accounted for in the occupied states.[34−36]

In order to directly probe the electronic structure of MoS_2, specifically the unoccupied density of states, scanning transmission X-ray microscopy (STXM) has been used to image a few-layered 2H-MoS_2 samples prepared by exfoliation of a single-crystal MoS_2 sample, as depicted in Figure 2. STXM provides a hyperspectral map of element-specific X-ray absorption (at the S $L_{2,3}$-edge in this case) with a pixel size of 30 nm × 30 nm and is obtained by raster scanning a finely focused and highly monochromatic incident soft X-ray beam across the sample.[37−40] As a first approximation, STXM provides a spatially localized view of the atom-projected density of states; the strong hybridization of S 3p and Mo 4d states at the conduction band edge can thus be directly probed at the S $L_{2,3}$-edge. Figure 2A illustrates an integrated STXM image of a ca. 45 nm thick (corresponding to about 60 layers assuming a layer thickness of 0.8 nm)[41] 2H-MoS_2 sample laying on a silicon nitride window, with Figure 2B showing the corresponding topographic atomic force microscopy (AFM) image and cross-sectional profile for this exfoliated flake. Figure 2D plots the integrated sulfur $L_{2,3}$-edge X-ray absorption spectrum measured across the flake. The sulfur L-edge comprises two spectral envelopes labeled as such in Figure 2D; a pre-edge region involving transitions from S $2p_{3/2}$ + $2p_{1/2}$ states → S 3p (ca. 162−165 eV, hybridized with Mo 4d states) and a much more intense primary absorption edge corresponding to S $2p_{3/2}$ + $2p_{1/2}$ → S 4d (ca. 167−180 eV, hybridized with Mo 5p states) transitions. Notably, the selection rules for X-ray absorption spectroscopy (change of angular momentum quantum number $\Delta l = \pm 1$; no change of spin) explain the much diminished intensity of the pre-edge absorption feature as compared to the primary absorption. The former feature is symmetry forbidden but observed as a result of the local breaking of symmetry[42] as well as hybridization of S 3p and Mo 4d states; in contrast, the p−d whiteline absorption is symmetry allowed.

Figure 2D shows a theoretical S-$L_{2,3}$-edge spectrum modeled using the XCH-XAS method[31] for the monolayer 2H-MoS_2

DOI: 10.1021/acscentsci.8b00042
ACS Cent. Sci. 2018, 4, 493−503

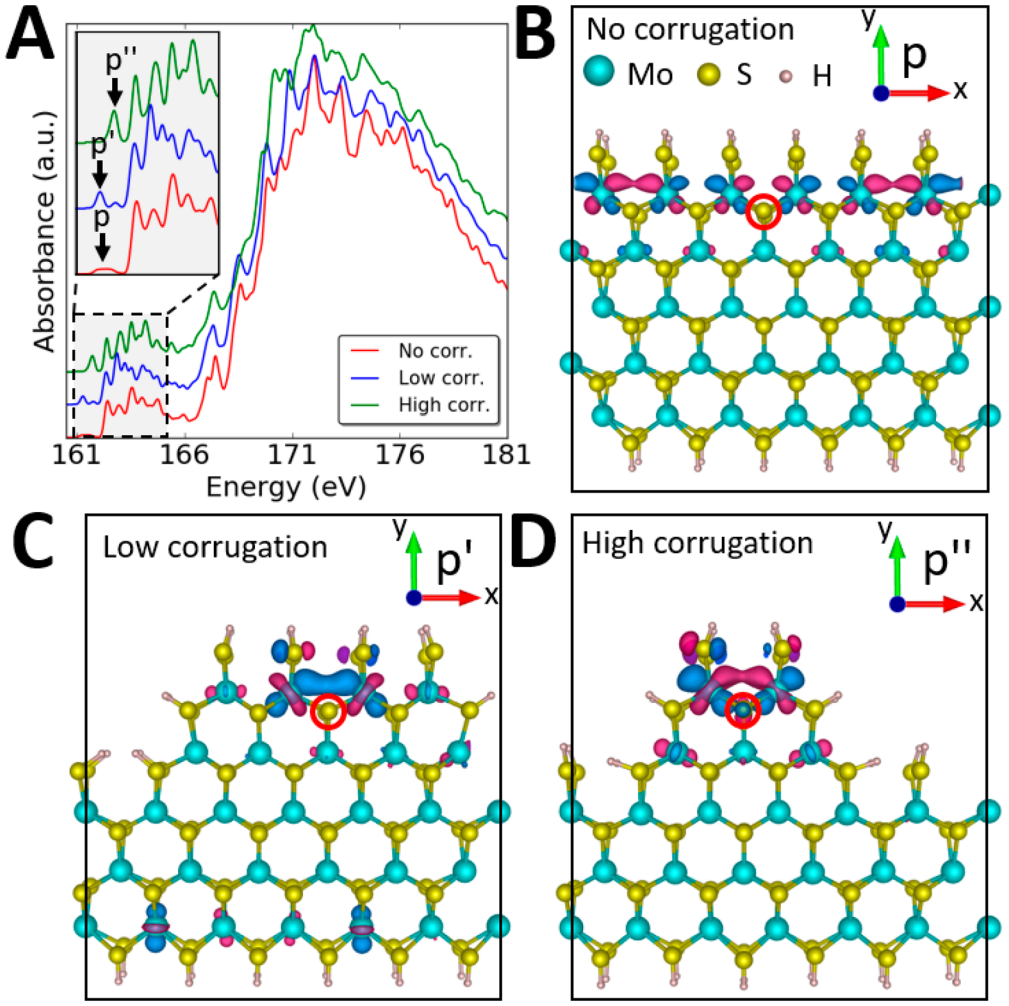

Figure 3. Influence of edge corrugation on S $L_{2,3}$-edge X-ray absorption spectra. (A) Comparison of simulated S $L_{2,3}$-edge X-ray absorption spectra for various degrees of edge corrugation. The inset shows an expanded view of the pre-edge region. With increasing extent of corrugation as depicted in panels (B), (C), and (D), the absorption feature delineated by an arrow increases in intensity. The orbital character for the emergent absorption feature demarcated with an arrow in (A) is shown for MoS_2 with (B) an intact edge; (C) partial edge corrugation; and (D) substantial edge corrugation. Mo atoms are depicted as light blue spheres and S atoms as yellow spheres. Opposite phases of the wave functions are represented as violet and dark blue lobes. In panels (B), (C), and (D), the excited sulfur atoms are delineated by red circles.

supercell depicted in Figure 2C along with the experimental spectrum. It is worth noting that in van der Waals' solid such as MoS_2, the calculated spectra for monolayer MoS_2 and bulk MoS_2 are closely concordant (as illustrated in Figure S3 of the Supporting Information) since element-specific XAS methods probe local structure, and the layers of multilayered samples are 3.22 Å apart. The simulated spectrum shows good agreement with the experimental spectrum and provides insight into the specific transitions and final states involved at this edge. Owing to atomic core-level spin−orbit coupling, the electrons can be excited from either $2p_{3/2}$ or $2p_{1/2}$ core levels of sulfur atoms, which results in splitting of the absorption features. Assuming the probability of excitation from a $2p_{1/2}$ core level is half of that from the $2p_{3/2}$ core level, which assumes the ground state population ratio of four $2p_{3/2}$ vs two $2p_{1/2}$ electrons, the total spectrum is modeled by using the following equation:

$$I_{\text{total}}(E) = I_0(E) + \frac{1}{2}I_0(E - \Delta S) + c \quad (1)$$

where $I_{\text{total}}(E)$ is the total intensity of the simulated spectrum, $I_0(E)$ is the intensity due to excitations from the $2p_{3/2}$ core level, E is the energy, ΔS is the spin−orbit coupling constant (which is 1.2 eV for sulfur),[43] and c is the constant added to the overall spectrum (158.7 eV in our case). Figure S4A (Supporting Information) schematically depicts excitations from $2p_{3/2}$ and $2p_{1/2}$ core levels to unoccupied electronic states. The total intensity of the simulated spectrum with the distinctive contributions from $2p_{3/2}$ and $2p_{1/2}$ core levels is shown in Figure S4B (Supporting Information).

Isosurfaces representing the square of the wave functions, corresponding to the charge density distribution of final states giving rise to the absorption features *a*−*i* in the sulfur $L_{2,3}$-edge XANES spectrum, have been plotted in Figure S5 (Supporting Information). Visualizing these isosurfaces and analyzing their orbital character facilitates chemically meaningful assignment of the spectral features. Also, as discernible from comparison with the atom-projected density of states in Figure 1C,D, the absorption features labeled *a*, *c*, and *e* in the pre-edge region correspond to transitions to final states that comprise S 3p character hybridized with Mo 4d states. For instance, in Figure S5B-a (Supporting Information), the lowest energy pre-edge absorption labeled *a* at 162.4 eV is attributed to an excited state with Mo 4d character, localized on three Mo atoms, which is furthermore hybridized with S 3p states localized on the excited

DOI: 10.1021/acscentsci.8b00042
ACS Cent. Sci. 2018, 4, 493−503

sulfur atom. A quantitative analysis of the orbital projected density of states reveals that this absorption feature has 16.6% Mo $4d_{xy}$, 26.0% Mo $4d_{z^2}$, and 16.5% Mo $4d_{x^2-y^2}$ character as the major contributors, as listed in Table S1 (Supporting Information). The percentage contribution of the excited S atom (red circle in Figure 2C) to the total DOS is shown in parentheses in Table S1 (Supporting Information). In contrast, the pre-edge feature *c* at 163.5 eV (Figure S5B-c) has primarily Mo 4d character delocalized across all the Mo atoms in the supercell with relatively little hybridization with S 3p states. The pre-edge feature labeled *e* at 164.8 eV (Figure S5B-e) is again attributed to excited Mo 4d states, delocalized across all molybdenum atoms in the supercell, which are further hybridized with S 3p states. The excited state corresponding to this absorption feature has 22.0% Mo $4d_{xz}$, 22.0% M $4d_{yz}$, 17.7% S $3p_x$, and 17.7% S $3p_y$ character.

The next set of absorption features, *f*—*i*, arises from dipole-allowed excitations of the S 2p core level electrons to states with substantial S 4d character. For instance, the feature *f* at 167.5 eV (Figure S5B-f, Supporting Information) corresponds to an excited state with S 4d character, localized on two adjacent S atoms and is predominantly antibonding in nature. Table S1 specifies that this excited state has 23.7% S $4d_{xz}$, 23.2% S $4d_{yz}$, and 19.5% S $4d_{z^2}$ character with some hybridization with Mo 5p states. Similarly, the state that gives rise to the absorption feature *g* at 168.8 eV (Figure S5B-g) is highly localized on two S atoms and has S 4d character; a detailed analysis of the state confirms that it is 14% S $4d_{xz}$ and 17.8% S $4d_{z^2}$ in nature. The orbital contributions to each of the absorption features can thus be visualized, and quantitative contributions from specific orbitals can be parsed as depicted in Figure S5 and Table S1 (Supporting Information), respectively.

Given the strong contributions from Mo 4d states and their apparent delocalization at the conduction band edge (Figures 1 and S1; Table S1), we have examined the evolution of S $L_{2,3}$-edge XANES spectra with increasing edge corrugation as realistically expected in high-edge-density nanotextured MoS_2 samples such as typically used for catalytic studies.[44] Figure 3 depicts S $L_{2,3}$-edge XANES spectra for a continuous 2H-MoS_2 nanoribbon with three distinct degrees of corrugation: (i) Figure 3B depicts the case of a MoS_2 nanoribbon with continuous thiol-terminated edges and no explicit corrugation; (ii) Figure 3C depicts a broken edge with a continuous strip of four and five sulfur-coordinated Mo atoms as the edge and edge-proximate layers, respectively; finally, (iii) Figure 3D depicts a highly corrugated edge where just two Mo-centered polyhedra constitute the edge and four neighboring Mo-centered polyhedra define the edge-proximal layer. Edge corrugation is believed to play a particularly important role in mediating the electrocatalytic hydrogen evolution reaction.[44] Simulated sulfur $L_{2,3}$-edge XANES spectra for these three configurations are plotted in Figure 3A. Weaker dipole-forbidden transitions corresponding to S $2p_{3/2}$ + $2p_{1/2}$ states → S 3p (hybridized with Mo 4d states) and more intense dipole-allowed transitions corresponding to S $2p_{3/2}$ + $2p_{1/2}$ → S 4d (hybridized with Mo 5p states) are again observed. However, the calculations suggest some intriguing differences in the spectral signatures of the three configurations at the lower edge of the conduction band in the spectral energy range from 161.3—161.7 eV, i.e., at the absorption onset, just below the pre-edge region. These features are marked in Figure 3A as *p*, *p*′, and *p*″ for the three edge configurations; the predicted intensity scales with increasing corrugation as $p < p' < p''$. The final state corresponding to the absorption feature denoted *p* at 161.4 eV (red curve in Figure 3A) for an uncorrugated MoS_2 nanoribbon can be attributed to a delocalized state, spanning all of the edge Mo atoms, with predominantly Mo 4d character. Table S2 (Supporting Information) suggests that the state comprises 20.0% Mo $4d_{xy}$, 13.1% Mo $4d_{z^2}$, 12.4% Mo $4d_{x^2-y^2}$, and 30.1% S $3p_y$ orbitals as the major contributors. Adjacent molybdenum atom pairs appear to interact through bonding interactions. In contrast, the more intense feature *p*′ at 161.3 eV (blue curve in Figure 3A) predicted for the MoS_2 monolayer with a corrugated edge is associated with excited states of Mo 4d character that are now localized on a single pair of Mo atoms at the edge and are hybridized to 3p states of the edge S atoms (Figure 3C). Similarly, the feature *p*″ at 161.7 eV (green curve in Figure 3A) predicted for highly corrugated MoS_2 is again Mo 4d in nature and is strongly localized on the two edge Mo atoms and hybridized with the 3p states of the four edge sulfur atoms (Figure 3D). Table S2 suggests that this state has 20.7% Mo $4d_{xy}$, 25.1% Mo $4d_{z^2}$, 16.1% Mo $4d_{x^2-y^2}$, and 22.4% S $3p_y$ character. The expected intensity differences can be rationalized considering that the X-ray absorption cross-section is dependent on the coupling between the initial state (2p eigenstate of the S atom) and the final state.[31] Since the initial 2p eigenstate is localized on an excited S atom, overlap with the final state will be the greatest if the final state is also localized. Consequently, delocalization of the final state across an extended array of Mo atoms, as expected for uncorrugated MoS_2 sheets (Figure 3B), will result in relatively weak coupling and thus low intensity of the corresponding edge feature, *p*; indeed, this feature is indistinguishable in S $L_{2,3}$-edge spectra acquired for an exfoliated few-layered MoS_2 sample shown in Figure 2. In contrast, extensive localization, as indicated for the highly corrugated edge configuration illustrated in Figure 3D, is expected to yield a low-energy spectral feature, *p*″, of much greater intensity. Indeed, this analysis reveals that corrugated edge sites such as depicted in Figure 3C,D that are thought to be catalytically active[44] have spectroscopically distinguishable signatures in the $S_{2,3}$ L-edge X-ray absorption spectra. According to a study by Liu and co-workers,[45] the dilute adsorption of hydrogen on metal chalcogenide surfaces has a negligible effect on its total electronic structure (DOS). However, the primary consequence of hydrogen adsorption is the population of states at or near the lowest unoccupied state, i.e., the conduction band minimum for semiconductors or the Fermi level for metals. Consequently, one strategy to increase the activity of a catalytic site (reflected in a decrease of its overpotential) in a semiconducting catalyst would be to decrease the energy of the conduction band minimum. In the case of MoS_2, the creation of edge defects has this very effect. Figure S6 (Supporting Information) indicates that the upon the inclusion of edges in a semi-infinite MoS_2 strip, "mid gap" states start to appear in the band gap and the conduction band minimum is lowered by 1.2 eV in comparison to monolayer 2H-MoS_2. The catalytic reactivity of the edges of MoS_2 catalysts is thus a direct reflection of this modified electronic structure.

As the mechanically exfoliated MoS_2 depicted in Figure 2 exhibited a low concentration of edge sites and barely discernible spectroscopic signatures of edge states, we have further examined a high-edge-density nanotextured MoS_2 sample prepared by calcination of $(NH_4)_2MoS_4$ solution on carbon fiber paper at 300 °C that is known to exhibit excellent electrocatalytic activity.[27] Extensive previous structural characterization of this sample suggests a mixture of amorphous and

DOI: 10.1021/acscentsci.8b00042
ACS Cent. Sci. 2018, 4, 493−503

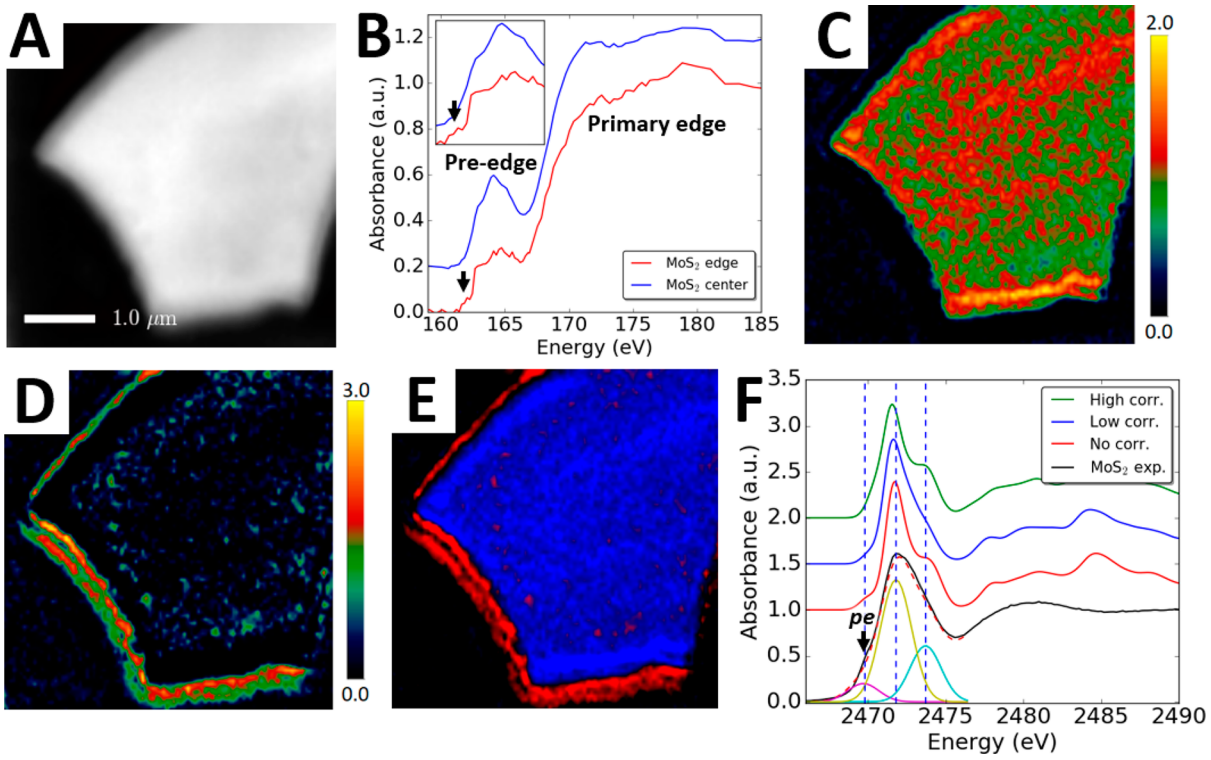

Figure 4. Mapping edge spectral signatures across a high-edge-density nanostructured MoS_2 sample. (A) Integrated S $L_{2,3}$-edge STXM image acquired for a high-edge-density MoS_2 nanosheet; (B) two spectral components that contribute to the overall integrated spectrum as derived from singular variable decomposition of the hyperspectral data based on region of interest analysis; (C) intensity map for the spectral contribution shown in the blue spectrum of panel (B) (corresponding to uncorrugated MoS_2); (D) intensity map for the spectral contribution shown in the red spectrum of panel (B) (corresponding to edge electronic states). In (C) and (D), the color bars to the right depict the relative intensity of the spectrum at each pixel. (E) False color map showing the relative spatial localization of the two spectral features; the color at each pixel represents the majority spectral contribution (red or blue as delineated by the plots in (B)). (F) Comparison of experimental S K-edge XANES spectrum (black) acquired for a high-edge-density MoS_2 nanosheet compared to spectra calculated for the three configurations with varying edge corrugation depicted in Figure 3B–D. Three distinct features are deconvoluted centered at 2469.8, 2471.8, and 2473.7 eV. The lowest energy pre-edge feature is delineated as "pe" using an arrow.

crystalline phases with incipient crystalline MoS_2 nuclei characterized by a high density of edge sites embedded within an amorphous matrix.[27,46,47] Figure 4A depicts the integrated S $L_{2,3}$-edge STXM image acquired for the sample transferred onto a silicon nitride grid. The edges and the center of the lamellar sheet are clearly discernible from the background. Singular value decomposition based on region-of-interest analysis allows for identification of two distinct spectral components as shown in Figure 4B. Both spectra show distinctive dipole-forbidden pre-edge and more intense dipole-allowed primary edge features as also observed (and assigned in Figure S3 and Table S1) for the mechanically exfoliated few-layered MoS_2 sheet in Figure 2. Upon comparing the blue and the red spectra in Figure 4B, a low-energy feature is clearly distinguishable in the range between 161.4 and 162.4 eV (centered at ca. 161.9 eV) and is delineated by an arrow. On the basis of predictions of the energy positioning of spectral features derived from corrugated edge states in Figure 3 and Table S2, this feature likely has an origin in localized edge electronic states. Indeed, spatial mapping of the two spectral components depicted in Figures 4C–E clearly indicates that the red spectral component, which has the additional edge spectroscopic signatures, is indeed strongly localized at the edges of the sheets as well as within specific domains within the interior, whereas the blue spectroscopic component is predominant within the interior of the sheet. Figure 4E depicts the relative spatial localization of the components and demarcates the clear segregation of the spectral signatures corresponding to distinctive electronic structures of edge corrugated and uncorrugated MoS_2 in real space.

Considering that S $L_{2,3}$-edge XANES spectra serve as an excellent probe of S 3p—Mo 4d hybridization, S K-edge XANES spectra have furthermore been acquired for the high-edge density MoS_2 sample, as plotted in Figure 4F, in order to serve as an additional independent probe of the S 3p states. Spectral simulations have been performed using the XCH-XAS method to facilitate spectral assignments. Two sets of absorption features can be distinguished corresponding to (i) dipolar transitions from S 1s core states to S 3p states hybridized with Mo 4d states in the energy range between ca. 2468–2476 eV and (ii) less intense dipole-forbidden transitions from S 1s core states to S 4d states in the energy range above 2476 eV, observed due to breaking of symmetry and p—d hybridization. Figure S7 (Supporting Information) depicts the final state assignments of the spectral features observed in S K-edge XANES spectra of monolayer 2H-MoS_2.

Interestingly, three discrete spectral components can be resolved in the experimental S K-edge XANES spectrum centered at 2469.8, 2471.8, and 2473.7 eV (Figure 4F). A distinctive pre-edge feature (denoted as *pe*) is observed at 2469.8 eV as demarcated by an arrow. As per Figure S7, such a spectral feature is not characteristic or expected for monolayer

DOI: 10.1021/acscentsci.8b00042
ACS Cent. Sci. 2018, 4, 493–503

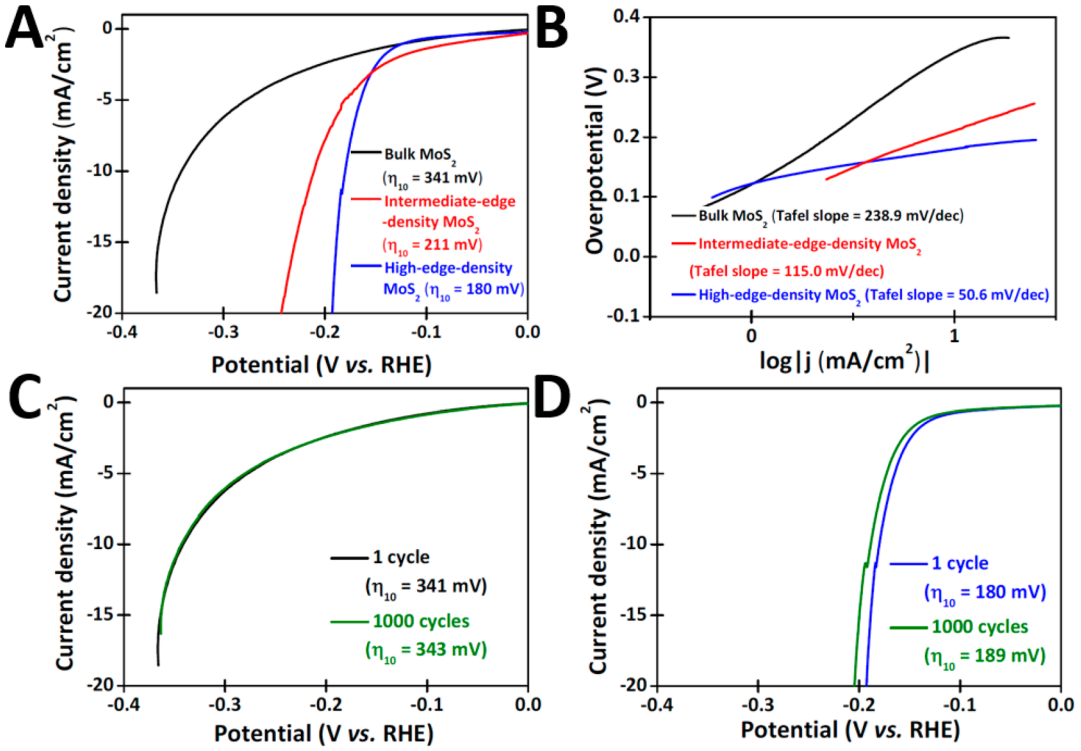

Figure 5. Contrasting electrocatalytic activity of bulk 2H-MoS_2, intermediate-edge-density nanostructured MoS_2, and high-edge-density nanostructured MoS_2. (A) Polarization curves and (B) Tafel plots contrasted for bulk 2H-MoS_2, intermediate-edge-density MoS_2, and high-edge-density MoS_2 integrated onto carbon fiber paper. The overpotentials (η_{10}), required to reach a current density of 10 mA/cm^2 as well as the Tafel slope values are noted. The overpotentials have been corrected for internal resistance losses. Electrocatalytic testing has been performed in a 0.5 M aqueous solution of H_2SO_4 using a three-electrode system. (C) and (D) polarization curves of bulk 2H-MoS_2 and high-edge-density MoS_2 before and after scanning across 1000 cyclic voltammetry cycles between −0.2 and 0.2 V versus RHE at a scan rate of 100 mV/s.

2H-MoS_2. In order to delve into the origin of this feature, S K-edge X-ray absorption spectra have been further modeled for the three distinctive edge corrugation modes considered in Figure 3B−D and are plotted alongside the experimental spectrum in Figure 4F. Indeed, a pre-edge feature is seen to emerge with increasing extent of corrugation. Figure S8 depicts the final states giving rise to pre-edge features in the calculated spectra for the three corrugation motifs. Similar to observations of the S $L_{2,3}$-edge XANES spectra, increasing corrugation brings about localization of the S 3p—Mo 4d states, and such a localized hybrid state yields a more intense pre-edge absorption. The independent identification of spectral signatures assigned to defective edge electronic structure in both S $L_{2,3}$- and S K-edge XANES spectra, the distinctive localization of such spectral features at nanostructured edges evidenced in S $L_{2,3}$-edge STXM imaging, and their much-increased abundance in a high-edge-density sample thus lend strong credence to the distinctive chemical bonding and electronic character of the edge states of MoS_2. Indeed, the abundance of edge states has been extensively correlated to the catalytic activity of MoS_2.[8,26,29,44]

The high-edge-density nanostructured MoS_2 sample exhibiting distinct spectral signatures of edge corrugation (Figure 4) has been evaluated for its efficacy as an electrocatalyst. A three-electrode system is assembled with high-edge-density MoS_2 on carbon fiber paper as the working electrode, SCE as the reference electrode, and a Pt plate as the counter electrode; a 0.5 M aqueous solution of H_2SO_4 is used as the electrolyte. While previous studies have provided an important caveat regarding the use of Pt as a counter-electrode,[48] Figure S9 of the Supporting Information illustrates that no discernible difference in electrocatalytic activity is observed within the limits of experimental error when a glassy carbon electrode is used instead of Pt as the counter electrode. The electrocatalytic activity of this sample is contrasted to bulk 2H-MoS_2 which has micron-sized crystalline domains and a substantially reduced edge density. Figure 5A,B contrasts the polarization curves and Tafel slopes for bulk 2H-MoS_2, intermediate-edge-density MoS_2, and high-edge-density MoS_2 integrated onto carbon fiber paper. The edge density is controlled by choice of annealing temperature; a higher annealing temperature results in sintering of incipient MoS_2 domains reducing the edge density as larger crystalline sheets are stabilized.[27] The exchange current density (a measure of the rate of electrochemical reaction at equilibrium)[49] for high-edge-density MoS_2 is far greater at a given overpotential as compared to bulk 2H-MoS_2. The overpotential (η_{10}), required to reach a current density of 10 mA cm^{-2} for bulk MoS_2 (341 mV) is reduced for intermediate-edge-density MoS_2 (211 mV), and furthermore reduced for the high-edge density MoS_2 sample (180 mV). Remarkably, the Tafel slope for the high-edge density MoS_2 sample (50.6 mV/dec) is substantially lower in comparison to the corresponding value for intermediate-edge-density MoS_2 (115.0 mV/dec) as well as for bulk MoS_2 (238.9 mV/dec). The substantial enhancement of the electrocataytic activity can be correlated to increased edge density, and thus suggests that the localized edge electronic states, with energies at the edge of the conduction band comprising localized Mo 4d—S 3p states, play a key role in catalysis. In fact, the excellent catalytic activity of cubane-like $[Mo_3S_4]^{4+}$ units reported in the literature is likely

DOI: 10.1021/acscentsci.8b00042
ACS Cent. Sci. 2018, 4, 493−503

related to the realization of a similar electronic structure motif characterized by such localized states.[50]

To further investigate the long-term stability of the samples, cyclic voltammetry measurements have been performed over 1000 cycles in a 0.5 M aqueous solution of H_2SO_4 between a potential range of −0.2 and 0.2 V versus RHE at a scan rate of 100 mV/s. Figure 5C,D suggests excellent retention of the electrocatalytic activity with only marginal degradation of the samples. The increase in η_{10} after 1000 cycles for high-edge-density MoS_2 is less than ca. 5 mV.

3. EXPERIMENTAL SECTION

3.1. Electronic Structure Calculations and Modeling of XAS Signatures. First-principles calculations were performed using density functional theory, as implemented within the Vienna *ab initio* simulation package (VASP).[51−53] The projector augmented wave (PAW) formalism was used to model electron−ion interactions. A kinetic energy cutoff of 600 eV was used for plane wave basis restriction. Electronic exchange and correlation effects were included using the generalized gradient approximation based on the Perdew−Burke−Ernzerhof functional (GGA-PBE).[54] For geometry optimization, the supercells of MoS_2 were relaxed until the Cartesian components of the forces were below ±0.05 eV $Å^{-1}$.

The PWscf code in the Quantum ESPRESSO package was used to calculate the excited state density of states (DOS) and projected density of states (PDOS) and to simulate X-ray absorption spectra. The Shirley optimal basis set was used to facilitate efficient sampling of the Brillouin zone.[55,56] For DOS and PDOS calculations, a uniform Γ-centered 4 × 4 × 4 Monkhorst−Pack k-point grid was used.[57] A uniform k-point grid of 2 × 2 × 2 was used to perform structural relaxations and simulate S K- and $L_{2,3}$-edge XANES spectra. The spectral simulation uses the XCH-XAS approach wherein an electron is removed from the inner shell (1s for S K-edge or 2p for S L-edge) of an excited sulfur atom within a MoS_2 supercell to account for excited state core−hole interactions.[31] The inclusion of the core−hole perturbation is not explicit but is instead accounted for using a modified sulfur pseudopotential with one less electron in the 1s orbital for the S K-edge or 2p orbital for the S L-edge. The excited electron is included in the occupied electronic structure, and the entire electronic system is relaxed to its ground state within DFT. A 4 × 4 × 4 supercell was used for the calculations of the electronic properties of the 2H-MoS_2 monolayer. A vacuum separation of 10 Å was used along the z direction to eliminate interactions between the slabs. For the calculation of edge corrugation effects, nanoribbons of MoS_2 extended periodically in the x-direction were used with thiol-terminated edges. A vacuum separation of 10 Å was inserted along the y-direction to eliminate interactions between the edges of MoS_2 nanoribbons in adjacent cells. The selected supercell was large enough to eliminate spurious interactions arising from coupling between core−hole images. A broadening of 0.2 eV was applied to spectral simulations in order to reproduce instrumental broadening observed in experimental spectra.

3.2. Material Synthesis. *3.2.1. Synthesis of Few-Layered 2H-MoS_2.* Few-layered MoS_2 nanosheets were deposited onto silicon nitride surfaces using mechanical exfoliation.[58] First, silicon nitride windows (Norcada, thickness 50 μm) were cleaned by using UV/ozone for 10 min to yield hydrophilic surfaces. The windows were then rinsed with deionized water and ethanol and dried under flowing nitrogen. Adhesive tape (Scotch Brand) was applied onto a MoS_2 crystal (SPI Supplies). After peeling, the tape was reapplied to the silicon nitride windows. The tape-MoS_2-window samples were annealed at 80 °C for 2 min to release any trapped gas at the MoS_2-substrate interface and improve the deposition efficiency.[59] After the samples were cooled to room temperature, the tape was peeled from the substrate, leaving MoS_2 flakes on the silicon nitride windows.

3.2.2. Synthesis of Nanostructured Intermediate-Edge-Density and High-Edge-Density MoS_2. Nanostructured MoS_2 was synthesized using a previously described procedure starting from an amorphous MoS_2 precursor.[27] Briefly, 0.25 g of ammonium thiomolybdate, $(NH_4)_2MoS_4$ (Sigma-Aldrich, 99.97% purity), was added to 20 mL of anhydrous dimethylformamide (DMF) under an argon atmosphere to obtain a 1.25 wt % solution. Next, after ultrasonication for 20 min, a 100 μL cm^{-2} solution was drop cast onto a carbon fiber paper substrate (Toray Paper 120). The substrate was then purged under an argon flow of 50 sccm for 20 min at room temperature and then calcined within a tube furnace at temperatures of 300 and 400 °C to obtain high-edge-density and intermediate-edge-density MoS_2, respectively. A ramp rate of 40 °C min^{-1} was used for calcination; the furnace was held at 300 °C/400 °C for 5 min before allowing the substrate to cool to room temperature. For STXM measurements, the sample was ultrasonicated in ethanol for 5 min, and the supernatant was drop cast onto silicon nitride windows (Norcada). Bulk MoS_2 powder with a particle size of ca. 2 μm was purchased from Sigma-Aldrich (99% purity) and used without further purification.

3.3. Atomic Force Microscopy, XAS, and STXM Measurements of MoS_2. The few-layered MoS_2 samples were examined by AFM using an Agilent 5500 AFM in a dry nitrogen environment. MicroMasch (CSC37/ALBS) silicon tips with a nominal spring constant of 1 N/m and a radius of curvature of ca. 12 nm were used to image the samples. AFM images were collected in contact mode at an applied load of 1 nN under a nitrogen atmosphere. Scanning probe image processing (SPIP) software was used to process the images and render topographical images.

STXM measurements were acquired at the S $L_{2,3}$-edge at beamline 10-ID1 of the Canadian Light Source (CLS) and at the 11.0.2 beamline of the Advance Light Source (ALS). The measurements used right circularly polarized light generated by an elliptically polarized undulator. A diffraction-limited spatial resolution of ca. 30 nm was obtained by using a 25 nm outermost-zone zone plate. Spectral stacks were acquired using a 500 line mm^{-1} plane grating monochromator (PGM). The incident photon flux (I_0) count rate was optimized to ca. 17 MHz as read by the STXM detector at 160 eV within a hole located in proximity of the sample of interest. The S L-edge stacks were collected in the energy range from 155 to 200 eV with energy steps of 0.2 eV in the region of interest and with energy steps 1 eV in the continuum region beyond the specific elemental edges; a dwell time of 1 ms was used for each spectral section. All STXM data were analyzed and processed using aXis2000 from McMaster University (http://unicorn.mcmaster.ca/aXis2000.html). STXM maps for spectral components were derived based on singular value decomposition of the image stack (performed in aXis2000) by using as a reference the total integrated spectrum.

Sulfur K-edge X-ray absorption near-edge structure (XANES) spectra were collected at the Advanced Light Source

DOI: 10.1021/acscentsci.8b00042
ACS Cent. Sci. 2018, 4, 493−503

(ALS) bending magnet beamline 10.3.2. S K-edge XANES spectra were recorded in fluorescence mode in the energy range 2450—2510 eV by continuously scanning a Si (111) monochromator (Quick XAS mode) from 20 eV below to 40 eV above the white line absorption. For XANES analysis, a suite of custom LabVIEW programs at the beamline was used to perform deadtime correction, energy calibration, glitch removal, pre-edge subtraction, and postedge normalization. The Athena suite of programs in the IFEFFIT package was used to analyze the XANES spectra.[60]

3.4. Evaluation of Electrocatalytic Activity. A three-electrode cell was constructed and cycled using a potentiostat (Bio-Logic, SP-200) with the MoS_2 active layer on carbon fiber paper as the working electrode. A 0.5 M aqueous solution of H_2SO_4 purged with N_2 gas was used as the electrolyte. A saturated calomel electrode (SCE) and a Pt plate were used as the reference and counter electrodes, respectively. Alternatively, glassy carbon was also used as a counter electrode to contrast with the Pt plate. The measurement of the polarization curves and the Tafel slope were recorded using both Pt and glassy carbon as counter electrodes. The expression $E_{RHE} = E_{SCE} + 0.279$ V was used to convert the potential measured versus SCE (E_{SCE}) to the potential versus the reversible hydrogen electrode (RHE, E_{RHE}).[12,27] Linear sweep voltammetry (LSV) was performed in the range between 0.1 and −0.4 V vs. RHE at a scan rate of 10 mV/s. Corrections were implemented to account for ohmic potential (iR) losses, where i is the current and R is the series resistance of the electrochemical cell, based on electrochemical impedance spectroscopy (EIS) measurements. A frequency range of 200 kHz to 50 mHz was used for the EIS measurements with an AC amplitude of 25 mV.

4. CONCLUSIONS

The electrocatalytic activity of MoS_2 has long been correlated to the abundance of edge sites. However, specific aspects of edge structure and their role in mediating catalysis remains unclear, thereby hampering the development of rational strategies for edge modification. In this article, using element-specific X-ray absorption spectroscopy to probe electronic structure in conjunction with first-principles DFT modeling of X-ray absorption spectra, we have shown that localization of Mo 4d—S 3p states at specific edge corrugations gives rise to distinctive edge electronic states. These edge states are spectroscopically distinguishable, independently, in both the S $L_{2,3}$- and K-edge XANES spectra. STXM imaging at the S $L_{2,3}$-edge indicates a pronounced abundance of such edge electronic states at the peripheries of high-edge density nanostructured MoS_2 samples; in contrast, such states were not observed for mechanically exfoliated MoS_2 flakes with large crystalline domains and a low abundance of edge sites. The presence of edge corrugation serves to disrupt extended delocalization of Mo 4d states and yields low-energy hybrid states at the edge of the conduction band. These states were found to correlate with substantially enhanced electrocatalytic activity, in terms of a lower Tafel slope and a higher exchange current density. Future work will focus on the rational design of schema for modulating the energy positioning and occupancies of these edge electronic states.

ASSOCIATED CONTENT

Supporting Information

The Supporting Information is available free of charge on the ACS Publications website at DOI: 10.1021/acscentsci.8b00042.

Figures depicting the methodology used for S L-edge calculation; density of states and atom projected density of states for monolayer 2H-MoS_2 and semi-infinite MoS_2 strip; orbital character of the final states observed in S L-edge and S K-edge spectra; tables showing the percentages of S and Mo character in excited states corresponding to specific intense absorption features observed in the S L-edge X-ray absorption spectra (PDF)

AUTHOR INFORMATION

Corresponding Authors

*(D.P.) E-mail: dgprendergast@lbl.gov.
*(S.B.) E-mail: banerjee@chem.tamu.edu.

ORCID

Yun-Hyuk Choi: 0000-0002-3120-1556
James D. Batteas: 0000-0002-6244-5000
Sarbajit Banerjee: 0000-0002-2028-4675

Notes

The authors declare no competing financial interest.

ACKNOWLEDGMENTS

The work was supported in part by a New Directions Award from the American Chemical Society Petroleum Research Fund (55315-ND10) and by the National Priorities Research Program award (NPRP9-160-2-088) from the Qatar National Research Fund. We acknowledge the Texas A&M Supercomputing Facility for computational resources. DFT simulations were performed as part of a User Project with DP at The Molecular Foundry (TMF), Lawrence Berkeley National Laboratory. T.M.F. is supported by the Office of Science, Office of Basic Energy Sciences, of the U.S. Department of Energy, under Contract No. DE-AC02- 05CH11231. J.D.B. acknowledges support from the National Science Foundation (CMMI-1436192). A.P. acknowledges support from the Advanced Light Source (ALS) doctoral fellowship in residence. The Advanced Light Source is supported by the Director, Office of Science, Office of Basic Energy Sciences, of the U.S. Department of Energy, under Contract No. DE-AC02-05CH11231.

REFERENCES

(1) Lewis, N. S.; Nocera, D. G. Powering the planet: Chemical challenges in solar energy utilization. *Proc. Natl. Acad. Sci. U. S. A.* **2006**, *103*, 15729−15735.
(2) Nocera, D. G. The artificial leaf. *Acc. Chem. Res.* **2012**, *45*, 767−776.
(3) Hisatomi, T.; Kubota, J.; Domen, K. Recent advances in semiconductors for photocatalytic and photoelectrochemical water splitting. *Chem. Soc. Rev.* **2014**, *43*, 7520−7535.
(4) Chen, X.; Shen, S.; Guo, L.; Mao, S. S. Semiconductor-based photocatalytic hydrogen generation. *Chem. Rev.* **2010**, *110*, 6503−6570.
(5) Bockris, J.; Ammar, I.; Huq, A. The mechanism of the hydrogen evolution reaction on platinum, silver and tungsten surfaces in acid solutions. *J. Phys. Chem.* **1957**, *61*, 879−886.
(6) Parsons, R. Hydrogen evolution on platinum electrodes. The heats of activation for the component reactions. *Trans. Faraday Soc.* **1960**, *56*, 1340−1350.
(7) Hinnemann, B.; Moses, P. G.; Bonde, J.; Jørgensen, K. P.; Nielsen, J. H.; Horch, S.; Chorkendorff, I.; Nørskov, J. K. Biomimetic Hydrogen Evolution: MoS_2 Nanoparticles as Catalyst for Hydrogen Evolution. *J. Am. Chem. Soc.* **2005**, *127*, 5308−5309.
(8) Jaramillo, T. F.; Jørgensen, K. P.; Bonde, J.; Nielsen, J. H.; Horch, S.; Chorkendorff, I. Identification of active edge sites for electro-

DOI: 10.1021/acscentsci.8b00042
ACS Cent. Sci. 2018, 4, 493−503

chemical H_2 evolution from MoS_2 nanocatalysts. *Science* **2007**, *317*, 100−102.
(9) Li, Y.; Wang, H.; Xie, L.; Liang, Y.; Hong, G.; Dai, H. MoS_2 nanoparticles grown on graphene: an advanced catalyst for the hydrogen evolution reaction. *J. Am. Chem. Soc.* **2011**, *133*, 7296−7299.
(10) Ye, G.; Gong, Y.; Lin, J.; Li, B.; He, Y.; Pantelides, S. T.; Zhou, W.; Vajtai, R.; Ajayan, P. M. Defects engineered monolayer MoS_2 for improved hydrogen evolution reaction. *Nano Lett.* **2016**, *16*, 1097−1103.
(11) Li, H.; Tsai, C.; Koh, A. L.; Cai, L.; Contryman, A. W.; Fragapane, A. H.; Zhao, J.; Han, H. S.; Manoharan, H. C.; Abild-Pedersen, F.; Nørskov, J. K.; Zheng, X. Activating and optimizing MoS_2 basal planes for hydrogen evolution through the formation of strained sulphur vacancies. *Nat. Mater.* **2016**, *15*, 48−53.
(12) Choi, Y.-H.; Lee, J.; Parija, A.; Cho, J.; Verkhoturov, S. V.; Al-Hashimi, M.; Fang, L.; Banerjee, S. An in Situ Sulfidation Approach for the Integration of MoS_2 Nanosheets on Carbon Fiber Paper and the Modulation of Its Electrocatalytic Activity by Interfacing with nC_{60}. *ACS Catal.* **2016**, *6*, 6246−6254.
(13) Gutiérrez, O. Y.; Singh, S.; Schachtl, E.; Kim, J.; Kondratieva, E.; Hein, J.; Lercher, J. A. Effects of the Support on the Performance and Promotion of (Ni)MoS_2 Catalysts for Simultaneous Hydrodenitrogenation and Hydrodesulfurization. *ACS Catal.* **2014**, *4*, 1487−1499.
(14) Rangarajan, S.; Mavrikakis, M. On the Preferred Active Sites of Promoted MoS_2 for Hydrodesulfurization with Minimal Organonitrogen Inhibition. *ACS Catal.* **2017**, *7*, 501−509.
(15) Bremmer, G. M.; van Haandel, L.; Hensen, E. J. M.; Frenken, J. W. M.; Kooyman, P. J. Instability of $NiMoS_2$ and $CoMoS_2$ Hydrodesulfurization Catalysts at Ambient Conditions: A Quasi in Situ High-Resolution Transmission Electron Microscopy and X-ray Photoelectron Spectroscopy Study. *J. Phys. Chem. C* **2016**, *120*, 19204−19211.
(16) Zhou, W.; Liu, M.; Zhou, Y.; Wei, Q.; Zhang, Q.; Ding, S.; Zhang, Y.; Yu, T.; You, Q. 4,6-Dimethyldibenzothiophene Hydrodesulfurization on Nickel-Modified USY-Supported NiMoS Catalysts: Effects of Modification Method. *Energy Fuels* **2017**, *31*, 7445−7455.
(17) Babu, G.; Masurkar, N.; Al Salem, H.; Arava, L. M. R. Transition Metal Dichalcogenide Atomic Layers for Lithium Polysulfides Electrocatalysis. *J. Am. Chem. Soc.* **2017**, *139*, 171−178.
(18) Tsai, C.; Abild-Pedersen, F.; Nørskov, J. K. Tuning the MoS_2 edge-site activity for hydrogen evolution via support interactions. *Nano Lett.* **2014**, *14*, 1381−1387.
(19) Fan, X.-L.; Yang, Y.; Xiao, P.; Lau, W.-M. Site-specific catalytic activity in exfoliated MoS_2 single-layer polytypes for hydrogen evolution: basal plane and edges. *J. Mater. Chem. A* **2014**, *2*, 20545−20551.
(20) Xiao, W.; Liu, P.; Zhang, J.; Song, W.; Feng, Y. P.; Gao, D.; Ding, J. Dual-Functional N Dopants in Edges and Basal Plane of MoS_2 Nanosheets Toward Efficient and Durable Hydrogen Evolution. *Adv. Energy Mater.* **2017**, *7*, 1602086.
(21) Bollinger, M.; Lauritsen, J.; Jacobsen, K. W.; Nørskov, J. K.; Helveg, S.; Besenbacher, F. One-dimensional metallic edge states in MoS_2. *Phys. Rev. Lett.* **2001**, *87*, 196803.
(22) Yang, Y.; Fei, H.; Ruan, G.; Xiang, C.; Tour, J. M. Edge-oriented MoS_2 nanoporous films as flexible electrodes for hydrogen evolution reactions and supercapacitor devices. *Adv. Mater.* **2014**, *26*, 8163−8168.
(23) Lauritsen, J. V.; Kibsgaard, J.; Helveg, S.; Topsoe, H.; Clausen, B. S.; Laegsgaard, E.; Besenbacher, F. Size-dependent structure of MoS_2 nanocrystals. *Nat. Nanotechnol.* **2007**, *2*, 53−58.
(24) Tsai, C.; Chan, K.; Abild-Pedersen, F.; Nørskov, J. K. Active edge sites in $MoSe_2$ and WSe_2 catalysts for the hydrogen evolution reaction: a density functional study. *Phys. Chem. Chem. Phys.* **2014**, *16*, 13156−13164.
(25) Voiry, D.; Salehi, M.; Silva, R.; Fujita, T.; Chen, M.; Asefa, T.; Shenoy, V. B.; Eda, G.; Chhowalla, M. Conducting MoS_2 nanosheets as catalysts for hydrogen evolution reaction. *Nano Lett.* **2013**, *13*, 6222−6227.
(26) Kibsgaard, J.; Chen, Z.; Reinecke, B. N.; Jaramillo, T. F. Engineering the surface structure of MoS_2 to preferentially expose active edge sites for electrocatalysis. *Nat. Mater.* **2012**, *11*, 963−969.
(27) Choi, Y.-H.; Cho, J.; Lunsford, A. M.; Al-Hashimi, M.; Fang, L.; Banerjee, S. Mapping the electrocatalytic activity of MoS_2 across its amorphous to crystalline transition. *J. Mater. Chem. A* **2017**, *5*, 5129−5141.
(28) Tinoco, M.; Maduro, L.; Masaki, M.; Okunishi, E.; Conesa-Boj, S. Strain-Dependent Edge Structures in MoS_2 Layers. *Nano Lett.* **2017**, *17*, 7021−7026.
(29) Lauritsen, J.; Nyberg, M.; Nørskov, J. K.; Clausen, B.; Topsøe, H.; Lægsgaard, E.; Besenbacher, F. Hydrodesulfurization reaction pathways on MoS_2 nanoclusters revealed by scanning tunneling microscopy. *J. Catal.* **2004**, *224*, 94−106.
(30) Bao, W.; Borys, N. J.; Ko, C.; Suh, J.; Fan, W.; Thron, A.; Zhang, Y.; Buyanin, A.; Zhang, J.; Cabrini, S.; Ashby, P. D.; Weber-Bargioni, A.; Tongay, S.; Aloni, S.; Ogletree, D. F.; Wu, J.; Salmeron, M. B.; Schuck, P. J. Visualizing nanoscale excitonic relaxation properties of disordered edges and grain boundaries in monolayer molybdenum disulfide. *Nat. Commun.* **2015**, *6*, 7993.
(31) Prendergast, D.; Galli, G. X-Ray Absorption Spectra of Water from First Principles Calculations. *Phys. Rev. Lett.* **2006**, *96*, 215502.
(32) Li, T.; Galli, G. Electronic Properties of MoS_2 Nanoparticles. *J. Phys. Chem. C* **2007**, *111*, 16192−16196.
(33) Mak, K. F.; Lee, C.; Hone, J.; Shan, J.; Heinz, T. F. Atomically thin MoS_2: a new direct-gap semiconductor. *Phys. Rev. Lett.* **2010**, *105*, 136805.
(34) Lukowski, M. A.; Daniel, A. S.; Meng, F.; Forticaux, A.; Li, L.; Jin, S. Enhanced hydrogen evolution catalysis from chemically exfoliated metallic MoS_2 nanosheets. *J. Am. Chem. Soc.* **2013**, *135*, 10274−10277.
(35) Lebegue, S.; Eriksson, O. Electronic structure of two-dimensional crystals from ab initio theory. *Phys. Rev. B: Condens. Matter Mater. Phys.* **2009**, *79*, 115409.
(36) Eknapakul, T.; King, P. D. C.; Asakawa, M.; Buaphet, P.; He, R. H.; Mo, S. K.; Takagi, H.; Shen, K. M.; Baumberger, F.; Sasagawa, T.; Jungthawan, S.; Meevasana, W. Electronic Structure of a Quasi-Freestanding MoS_2 Monolayer. *Nano Lett.* **2014**, *14*, 1312−1316.
(37) Ade, H.; Hitchcock, A. P. NEXAFS microscopy and resonant scattering: Composition and orientation probed in real and reciprocal space. *Polymer* **2008**, *49*, 643−675.
(38) Lim, J.; Li, Y.; Alsem, D. H.; So, H.; Lee, S. C.; Bai, P.; Cogswell, D. A.; Liu, X.; Jin, N.; Yu, Y.-s.; Salmon, N. J.; Shapiro, D. A.; Bazant, M. Z.; Tyliszczak, T.; Chueh, W. C. Origin and hysteresis of lithium compositional spatiodynamics within battery primary particles. *Science* **2016**, *353*, 566−571.
(39) De Jesus, L. R.; Horrocks, G. A.; Liang, Y.; Parija, A.; Jaye, C.; Wangoh, L.; Wang, J.; Fischer, D. A.; Piper, L. F.; Prendergast, D.; Banerjee, S. Mapping polaronic states and lithiation gradients in individual V_2O_5 nanowires. *Nat. Commun.* **2016**, *7*, 12022.
(40) Collins, B. A.; Ade, H. Quantitative compositional analysis of organic thin films using transmission NEXAFS spectroscopy in an X-ray microscope. *J. Electron Spectrosc. Relat. Phenom.* **2012**, *185*, 119−128.
(41) Lee, C.; Yan, H.; Brus, L. E.; Heinz, T. F.; Hone, J.; Ryu, S. Anomalous Lattice Vibrations of Single- and Few-Layer MoS_2. *ACS Nano* **2010**, *4*, 2695−2700.
(42) Yamamoto, T. Assignment of pre-edge peaks in K-edge x-ray absorption spectra of 3d transition metal compounds: electric dipole or quadrupole? *X-Ray Spectrom.* **2008**, *37*, 572−584.
(43) Han, S.; Kwon, H.; Kim, S. K.; Ryu, S.; Yun, W. S.; Kim, D.; Hwang, J.; Kang, J.-S.; Baik, J.; Shin, H.; Hong, S. C. Band-gap transition induced by interlayer van der Waals interaction in MoS_2. *Phys. Rev. B: Condens. Matter Mater. Phys.* **2011**, *84*, 045409.
(44) Benck, J. D.; Hellstern, T. R.; Kibsgaard, J.; Chakthranont, P.; Jaramillo, T. F. Catalyzing the hydrogen evolution reaction (HER) with molybdenum sulfide nanomaterials. *ACS Catal.* **2014**, *4*, 3957−3971.

DOI: 10.1021/acscentsci.8b00042
ACS Cent. Sci. 2018, 4, 493−503

(45) Liu, Y.; Wu, J.; Hackenberg, K. P.; Zhang, J.; Wang, Y. M.; Yang, Y.; Keyshar, K.; Gu, J.; Ogitsu, T.; Vajtai, R.; Lou, J.; Ajayan, P. M.; Wood, B. C.; Yakobson, B. I. Self-optimizing, highly surface-active layered metal dichalcogenide catalysts for hydrogen evolution. *Nat. Energy* **2017**, *2*, 17127.
(46) Li, H.; Zhang, Q.; Yap, C. C. R.; Tay, B. K.; Edwin, T. H. T.; Olivier, A.; Baillargeat, D. From bulk to monolayer MoS_2: evolution of Raman scattering. *Adv. Funct. Mater.* **2012**, *22*, 1385−1390.
(47) Lee, C.; Yan, H.; Brus, L. E.; Heinz, T. F.; Hone, J.; Ryu, S. Anomalous lattice vibrations of single-and few-layer MoS_2. *ACS Nano* **2010**, *4*, 2695−2700.
(48) Chen, R.; Yang, C.; Cai, W.; Wang, H.-Y.; Miao, J.; Zhang, L.; Chen, S.; Liu, B. Use of Platinum as the Counter Electrode to Study the Activity of Nonprecious Metal Catalysts for the Hydrogen Evolution Reaction. *ACS Energy Letters* **2017**, *2*, 1070−1075.
(49) Bose, R.; Balasingam, S. K.; Shin, S.; Jin, Z.; Kwon, D. H.; Jun, Y.; Min, Y.-S. Importance of hydrophilic pretreatment in the hydrothermal growth of amorphous molybdenum sulfide for hydrogen evolution catalysis. *Langmuir* **2015**, *31*, 5220−5227.
(50) Merki, D.; Hu, X. Recent developments of molybdenum and tungsten sulfides as hydrogen evolution catalysts. *Energy Environ. Sci.* **2011**, *4*, 3878−3888.
(51) Kresse, G.; Furthmüller, J. Efficiency of ab-initio total energy calculations for metals and semiconductors using a plane-wave basis set. *Comput. Mater. Sci.* **1996**, *6*, 15−50.
(52) Hohenberg, P.; Kohn, W. Inhomogeneous electron gas. *Phys. Rev.* **1964**, *136*, B864.
(53) Kohn, W.; Sham, L. J. Self-consistent equations including exchange and correlation effects. *Phys. Rev.* **1965**, *140*, A1133.
(54) Perdew, J. P.; Burke, K.; Ernzerhof, M. Generalized gradient approximation made simple. *Phys. Rev. Lett.* **1996**, *77*, 3865.
(55) Prendergast, D.; Louie, S. G. Bloch-state-based interpolation: An efficient generalization of the Shirley approach to interpolating electronic structure. *Phys. Rev. B: Condens. Matter Mater. Phys.* **2009**, *80*, 235126.
(56) Shirley, E. L. Optimal basis sets for detailed Brillouin-zone integrations. *Phys. Rev. B: Condens. Matter Mater. Phys.* **1996**, *54*, 16464.
(57) Monkhorst, H. J.; Pack, J. D. Special points for Brillouin-zone integrations. *Phys. Rev. B* **1976**, *13*, 5188.
(58) Novoselov, K. S.; Geim, A. K.; Morozov, S. V.; Jiang, D.; Zhang, Y.; Dubonos, S. V.; Grigorieva, I. V.; Firsov, A. A. Electric field effect in atomically thin carbon films. *Science* **2004**, *306*, 666−669.
(59) Huang, Y.; Sutter, E.; Shi, N. N.; Zheng, J.; Yang, T.; Englund, D.; Gao, H.-J.; Sutter, P. Reliable exfoliation of large-area high-quality flakes of graphene and other two-dimensional materials. *ACS Nano* **2015**, *9*, 10612−10620.
(60) Ravel, B.; Newville, M. ATHENA and ARTEMIS: interactive graphical data analysis using IFEFFIT. *Phys. Scr.* **2005**, *2005*, 1007.

DOI: 10.1021/acscentsci.8b00042
ACS Cent. Sci. 2018, 4, 493−503